Doped sol-gel based microstructured layers to improve the light emission of luminescent coatings

Léa Marichez, Geneviève Chadeyron, Daniel Zambon, François Réveret, Audrey Potdevin, Damien Boyer, Valentin Gaté, Isabelle Verrier, Damien Jamon, Emilie Gamet, et al.

▶ **To cite this version:**

Léa Marichez, Geneviève Chadeyron, Daniel Zambon, François Réveret, Audrey Potdevin, et al.. Doped sol-gel based microstructured layers to improve the light emission of luminescent coatings. Journal of Alloys and Compounds, 2023, 957, pp.170408. 10.1016/j.jallcom.2023.170408 . hal-04093898

HAL Id: hal-04093898

https://cnrs.hal.science/hal-04093898v1

Submitted on 14 Jun 2023

HAL is a multi-disciplinary open access archive for the deposit and dissemination of scientific research documents, whether they are published or not. The documents may come from teaching and research institutions in France or abroad, or from public or private research centers.

L'archive ouverte pluridisciplinaire **HAL**, est destinée au dépôt et à la diffusion de documents scientifiques de niveau recherche, publiés ou non, émanant des établissements d'enseignement et de recherche français ou étrangers, des laboratoires publics ou privés.

Doped sol-gel based microstructured layers to improve the light emission of luminescent coatings

Léa Marichez[1,2], Geneviève Chadeyron[2]*, Daniel Zambon[2]*, François Réveret[2], Audrey Potdevin[2], Damien Boyer[2], Valentin Gaté[3], Isabelle Verrier[1], Emilie Gamet[1], Yves Jourlin[1]

[1] *Laboratoire Hubert Curien UMR CNRS 5516, Université de Lyon, 18 Rue Professeur Benoît Lauras, 42000 Saint-Étienne, France*

[2.] *Université Clermont Auvergne, CNRS, Clermont Auvergne INP, ICCF, F-63000 Clermont–Ferrand, France.*

[3] *SILSEF, 382 Rue Louis Roustin, 74160 Archamps, France.*

Corresponding authors: genevieve.chadeyron@sigma-clermont.fr and daniel.zambon@uca.fr

Abstract

Sol-gel based layers doped with Rhodamine B phosphors (RB) were directly microstructured to produce sub-lambda 2D gratings, using nanoimprint lithography. Such an approach enables the simplification of technological processes, since no further etching process is required, which reduces considerably the number of technological steps and thus production costs. Surface microstructuring improved fluorophore emission in the visible range. Demonstrations were performed experimentally and samples were characterized using angle-resolved fluorescence. The emissions measured on microstructured luminescent coatings were 3 to 4 times higher, depending on the angle of observation, than those recorded on flat surfaces. This technological approach is very promising for the next generation of low-cost, high-performance anti-counterfeiting marking processes and for the traceability of objects based on unique optical effects.

Key Words: luminescent coating, microstructuring, nanoimprint lithography, diffraction grating.

1. Introduction

The fight against counterfeiting is very expensive for the global economy, and today all sectors of activity have to use marking and traceably technology to conform to regulatory requirements or respect good practices. A number of technologies exist, with varying costs or levels of security [1]. Even though these technologies are increasingly sophisticated, it is necessary to develop fast and cost-effective solutions with a higher security level. Luminescent marking [2] is an invisible marking technique (level 2) but it is easily counterfeited. Microstructuring, like hologram technology [2], is a visible marking process (level 1), but is much more difficult to counterfeit. Microstructuring on a luminescent coating is a promising approach since it can combine several optical effects, giving rise to unique markings which are difficult to reproduce or copy.

At the same time, nanoimprint technology enables the microstructuring of sol gel material layers without any other technological processes (etching, lithography…) [3–7]. Thus, combining luminescent material in a silica sol-gel before microstructuring by nanoimprint is a very promising technology route and a faster method, with high throughput structuring processes, that will be more easily adaptable for industrial deployment. There are many papers on the microstructuring of phosphor-doped sol-gel coatings [3, 4] for different applications, such as lighting [6-8] or solar cells [4]. Other authors, such as Pina-Hernandez et al [5] have developed a new method to produce printed active photonic devices using nanoimprint lithography, combining a printable high-refractive-index material and colloidal CdSe/CdS quantum dots (QDs) for applications in the visible region. Active media QDs were applied in two different ways: embedded inside a printable high-refractive-index matrix to form an active printable hybrid nanocomposite, and used as a uniform coating on top of printed photonic devices.

However, to the best of our knowledge, only a few papers report on the direct patterning of the doped sol-gel coating using nanoimprint technology. Indeed, Revaux et al [8] reported structured luminescent thin films with a doped sol-gel, but this concerned the upper and non-functional layer. In their study, the authors aim to microstructure the luminescent-based sol gel layer. This approach has two effects: the enhancement of the emitted luminescent light (visible light extraction) and increased UV light trapping in order to increase the number of incident photons in the luminescent layer (such as an anti-reflection coating).

They demonstrated a promising approach based on a doped sol-gel matrix with phosphor molecules, compatible with direct microstructuring using nanoimprint technology

[8]. First, in their paper, which concerns lighting applications, they used different phosphors to the ones we investigated in our study for anti-counterfeiting applications. Secondly, in our current paper, we optimized and micro-nanostructured, using the nanoimprint lithography (NIL) process, the whole sol-gel based functional layer for both light trapping and light extraction for a wider phosphor emission angle.

This article is organised in the following way: first, the different production steps are described, involving the synthesis of the fluorophore solutions and their mixture leading to layer deposition and grating printing. Next, the results of the measurements on the fabricated samples are discussed: different emission spectra and angle-resolved fluorescence are commented on, leading to the best choice of samples. The conclusion highlights the improvement in luminescence when using a micro-structured layer instead of a plane sample.

2. Experimental section

The fabricated sample is presented in Fig. 1 and the fabrication steps will be detailed later.

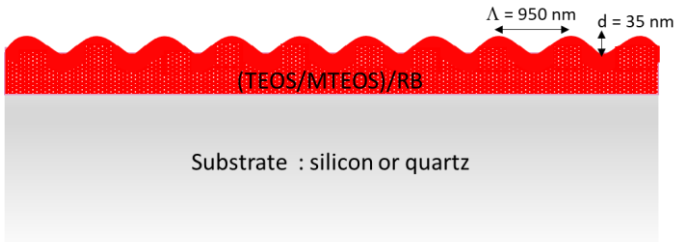

Fig. 1. Structure of the sample.

The sample consists of a silicon (or quartz) substrate with a luminescent sol-gel coating microstructured using the nanoimprint lithography technique. The latter consists of a tetraethoxysilane (TEOS)/methyltriethoxysilane (MTEOS) sol containing Rhodhamine B ((TEOS/MTEOS)/ RB). The pattern is a 2D sinusoidal diffraction grating.

2.1. Materials

Rhodamine B (RB) salt $C_{28}H_{31}ClN_2O_3$ and tetraethoxysilane (TEOS) of formula $Si(OCH_2\ CH_3\ )_4$ and methyltriethoxysilane (MTEOS) of formula $C_7H_{18}O_3Si$, with purities of at least 98% were purchased from Sigma-Aldrich. Table 1 gives the developed formulae of these precursors. Different types of substrates were used: quartz substrates and silicon wafers of 1 inch diameter were provided by Neyco.

Table 1: Names and developed formulae of precursors.

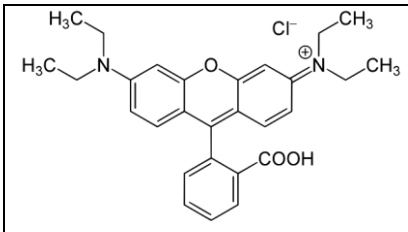	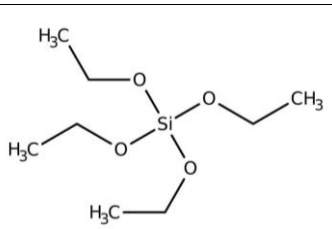	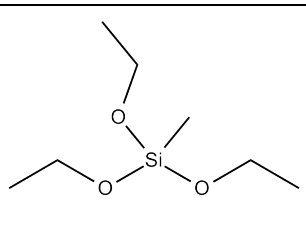
Rhodamine B : RB	Tetraethoxysilane : TEOS	Methyltriethoxysilane : MTEOS

2.2. Synthesis procedure of RB solutions and TEOS/MTEOS sol

Five solutions with RB concentrations ranging from 1.65 10^{-3} to 1.65 10^{-5} mol/L in ethanol were prepared in order to determine the concentration leading to the most interesting optical performance. The concentrations studied are reported in Table 2 and will be noted S_x (with x = 0 for the most concentrated solution to 4 for the most diluted solution). A

photograph of the solutions in daylight and under UV light is shown in figure S1; the luminescence of RB in ethanol solution under UV excitation at 365 nm is clearly revealed.

A solution in water/ethanol media using methyltriethoxysilane (MTEOS) and tetraethoxysilane (TEOS) as silica precursors was prepared by mixing the components in the following molar ratio: ethanol/water/silica precursors ((TEOS/MTEOS) 3/1): 4/1/0.25.

This sol, which will be used as a dispersion medium for RB, was formulated taking into account several physico-chemical parameters, such as its viscosity and the possibility of producing one-shot transparent coatings of a few hundred nanometres thickness by spin coating. The formulation was chosen based on the protocol presented in the work of Anastasova *et al.* [9] and Rios *et al.* [10]. Ethanol is used to adjust the viscosity.

Table 2: List of RB solution samples in ethanol and TEOS/MTEOS sol.

Concentration of RB in ethanol and TEOS /MTEOS sol (mol/L)	Solutions	Sols (TEOS/MTEOS)/RB
$1.65.10^{-3}$	S_0	S_{0T}
$3.29.10^{-4}$	S_1	S_{1T}
$1.65.10^{-4}$	S_2	S_{2T}
$3.29.10^{-5}$	S_3	S_{3T}
$1.65.10^{-5}$	S_4	S_{4T}

2.3. Synthesis of the (TEOS/MTEOS)/RB solutions

Several TEOS/MTEOS/RB sols were prepared by mixing RB ethanolic solutions in ethanol/water/TEOS/MTEOS sol media. RB amounts were calculated to keep the same concentrations as those given in Table 2 for $S_{0\text{-}4}$ ethanolic solutions. The solutions were homogenised with a magnetic stirrer for 18 hours at room temperature before being used to make thin films by spin coating. These sols present low viscosity and a yellow-orange luminescence similar to that of RB in ethanol under a UV excitation of 365 nm (Figure S1).

2.4. Elaboration of nanocomposite functional coatings

Nanocomposite coatings were elaborated using the spin-coating method. Spin-coating conditions, such as rotation speed and drying time, were optimized in order to obtain thin coatings (a few hundred nm) with a unique deposition. For this purpose, a 300 µL droplet of the S_{1T} suspension was deposited at 3000 rpm for 60s on quartz and silicon wafer substrates

with a drying time of 2 hours at 80°C to evaporate the solvent and allow the full polymerisation of the silica matrix. These films will hereafter be referred to as S_{1TR}. The thickness of the films was measured by profilometry and their surface roughness and topography were studied using Atomic Force Microscopy (AFM). A reference film without RB was prepared with the TEOS/MTEOS sol.

2.5. Elaboration of the diffraction gratings

The diffraction gratings were fabricated using the nanoimprint lithography process via three process steps. First, Laser Interferential photoLithography (LIL) was performed on a positive photoresist to create a grating master. Then, a PDMS mould was replicated from the master. Finally, the mould was used to print the master pattern directly onto the luminescent coating by nanoimprint lithography (NIL), performed by our industrial partner SILSEF.

2.6. Characterization techniques

The viscosity of RB solutions in ethanol and (TEOS/ MTEOS)/RB sols was measured with a Vibro Viscometer SV-A0/SV 100 after six days at a temperature of 18°C.

The thickness of the (TEOS/MTEOS)/RB thin films was measured using a Alpha Step IQ Profilometer from KLA Tencor. Three random locations on each film sample were used to determine the thickness.

AFM measurements were performed in tapping mode using a Nanoscope IIIa Atomic Force Microscope (AFM) from Veeco Instruments. The surface topographical images of the nanocomposite films obtained by AFM were worked up with Nanoscope 7.20 image processing software. RMS roughness (R_q) values for the surfaces, defined as the standard deviation of the z values within a given area, were calculated according to Equation (1)

$$(1)\ R_q = \sqrt{\frac{\sum(Z_t - Z_{ave})^2}{N}}$$

where z_{ave} is the average of the z values within the given area, z_t is the z value for a given point, and N is the number of points within the given area. Images of the films were obtained at three different locations, and four locations within each image were used to calculate the average roughness.

The optical indices (refractive index and extinction coefficient) were determined from phase-modulated spectroscopic ellipsometry measurements using a Jobin-Yvon UVISEL apparatus (0.59–4.79 eV and fixed 70° incident angle).

The UV–visible absorption spectra of the samples were recorded in the 200-800 nm wavelength range using a UV–vis spectrophotometer (SP-3000 Plus) equipped with an integrating sphere and UV-Probe software.

Quantum yield efficiencies and emission spectra were measured at room temperature using a C9920−02G PL-QY integrating sphere measurement system from Hamamatsu Photonics. The setup consisted of a 150 W monochromatic Xe lamp, an integrating sphere (Spectralon coating, ⌀ = 3.3 in.) and a high-sensitivity CCD camera. The internal photoluminescence quantum yield PL QY_{int} and the absorbance (Abs) defined by formulae 1 and 2 were obtained directly from the measurements made in the integrating sphere. The absolute photoluminescence quantum yield PL QY_{abs} was calculated from the product of PL QY_{int} * Abs, and corresponds to the number of emitted photons over the number of incident photons (formula (3)).

(1) PL QY_{int} = number of emitted photons/number of absorbed photons

(2) Abs = number of absorbed photons/number of incident photons

(3) PL QY_{abs} = PL QY_{int} . Abs = number of emitted photons/number of incident photons.

Angle-resolved photoluminescence was performed at room temperature. A 375 nm laser diode was used to excite the sample at 60° from normal incidence. The spot size was around 2 x 6 mm². The luminescence signal was detected by an optical fibre mounted on a goniometer to collect emissions from 0° (front of the sample) to 90° with an angular resolution of 0.9°. A 425 nm long pass filter was used to remove the excitation source on the detection line. The signal was then focused on the slit on a 32 cm focal monochromator and detected by a CCD camera.

Far-field emission measurements were carried out using a microscope lens with a numerical aperture of 0.55 giving access to a large range of emission angles (11.6° to 78.4°) with an angular resolution of 0.26°. The sample was optically pumped with a 375 nm laser diode with a spot diameter of 7 µm. The detection line was the same as with the angle-resolved photoluminescence setup.

3. Results and discussion

3.1. Screening for the best RB concentration in ethanol and in TEOS/MTEOS

3.1.1. Optical properties of RB ethanolic solution

Firstly, the optimal RB ethanolic solution leading to the best luminescence properties was established through the absolute photoluminescence quantum yield values (PL QY_{abs}). The corresponding PL QY_{abs} variation for S_2 solution (corresponding to $1.65.10^{-4}$ $mol.L^{-1}$) is given in Fig. 2a as a function of the excitation wavelength. Fig. S2 shows PL QY_{abs} curves for other RB solutions.

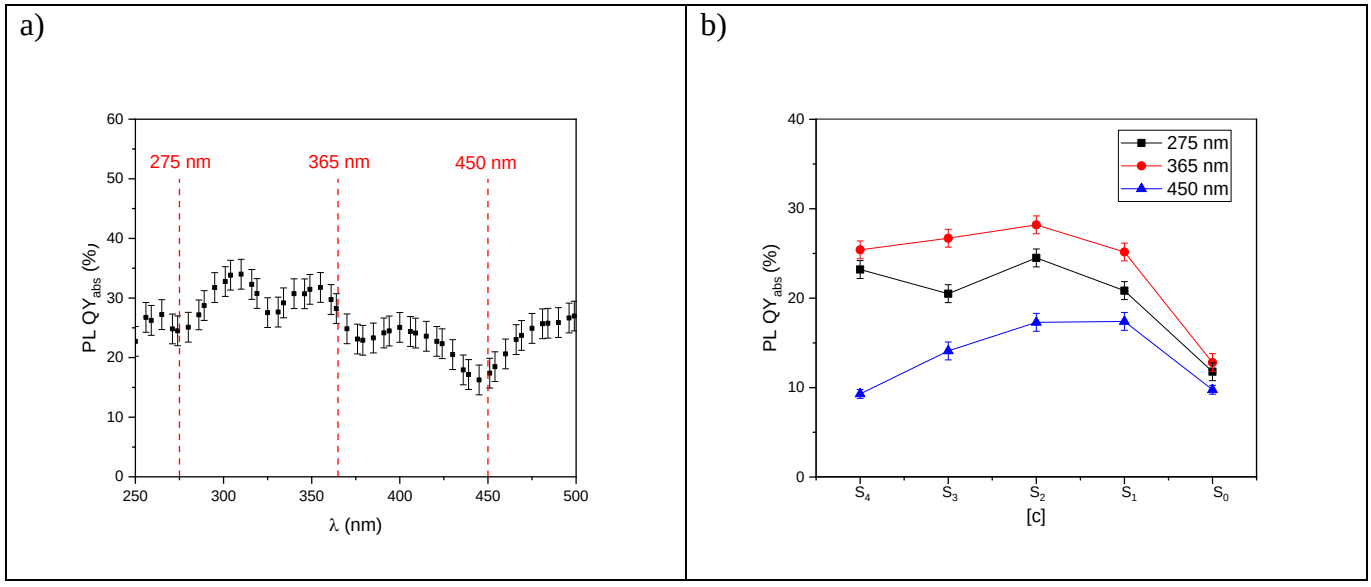

Fig. 2. a) Variation in PL QY_{abs} as a function of the excitation wavelength for solution S_2, b) Variation in PL QY_{abs} as a function of the RB solutions in ethanol ($S_{0, 1, 2, 3 \text{ and } 4}$) for λ_{exc} = 275, 365 and 450 nm.

Spectral profiles similar to that shown in Fig. 2a for S_2 solution were recorded whatever the RB concentration in ethanol except for the most concentrated one S_0 (Fig. S2a). For all the solutions studied (except S_0), the absolute photoluminescence quantum yields are between 20 and 35% on most of the range of excitation wavelengths investigated. We can therefore conclude that these solutions can be efficiently excited over a wide range of wavelengths and in particular by commercial UV and/or blue LEDs whose corresponding wavelengths 275, 365 and 450 nm are shown as dotted lines in Fig. 2a and S2.

For all these three wavelengths of interest, the PL QY_{abs} increases with the amount of RB in solution, then reaches a maximum for solutions with concentrations between S3 and S1, depending on the excitation wavelength, before decreasing again. This behaviour is observed whatever the considered excitation wavelength (Fig.2b). The best values are obtained for the 365 nm excitation.

The reduction in PL QY_{abs} when the RB amount becomes higher than 1.65 10^{-4} (solution S_2) could be explained by a concentration quenching phenomenon, which is predominant when the concentration of RB increases above a certain threshold. The same behaviour has been evidenced in the case of fluorescein and sulforhodamine (SRB) [11–13]. Indeed, when RB molecules are sufficiently close to each other, they are prone to aggregation by π-stacking (parallel stacking) due to conjugated xanthene rings or by hydrogen bonding (head-to-tail). Xanthene dyes such as RB, SRB or fluorescein are well known [14] to interact mutually, resulting in luminescence quenching when the concentration reaches a critical value to form dimers, trimers, etc.

Although the monomer yields luminescence properties, most aggregates led to the extinction of the optical properties due to non-radiative energy transfer between the dye molecules [15]. This phenomenon increases with the dye concentration in solution. All the excitation wavelengths studied result in an optimal PL QY_{abs} for a very low concentration of photoactive molecules in ethanolic solution.

In all cases, a compromise between a high internal photoluminescence quantum yield (isolated RB molecules in solution) (Fig. S3a) while maintaining an appropriate absorbance (Fig. S3b) (given for a significant amount of RB) must be reached.

3.1.2. Optical properties of RB in TEOS/MTEOS sol

The PL QY_{abs}, PL QY_{int} and absorbance of the different sols (TEOS/MTEOS)/RB recorded for the three excitation wavelengths corresponding to the commercial LEDs are shown in Fig. 3a, and S4a and b respectively for all prepared amounts. As observed for the RB ethanolic solutions (Fig. 2b) the best PL QY_{abs} values are obtained for an excitation wavelength of 365 nm.

a)	b)

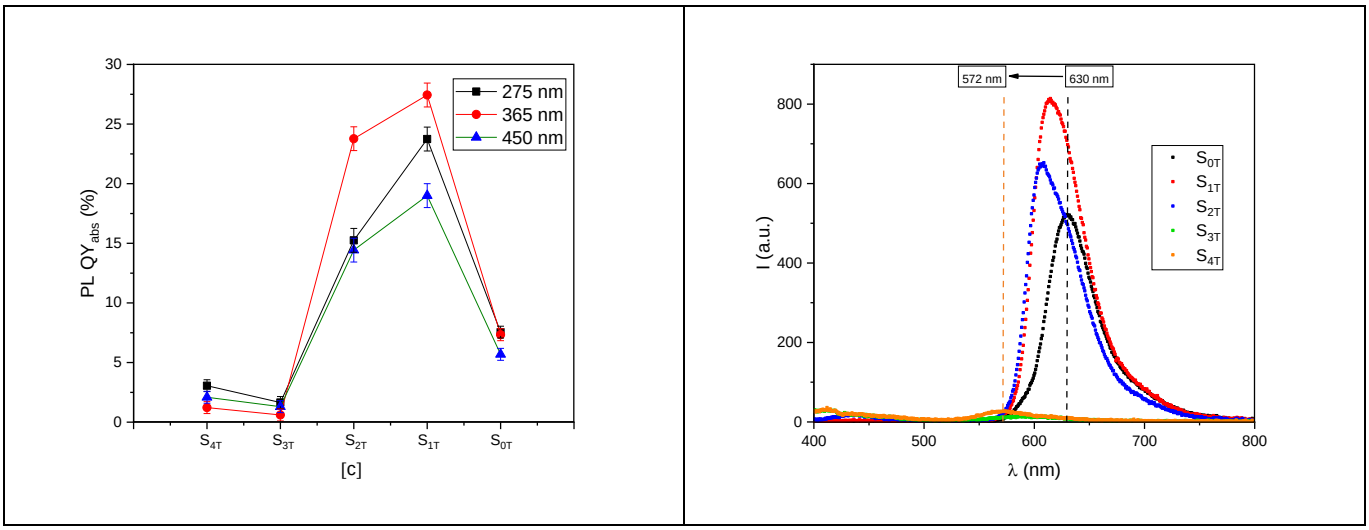

Fig. 3. a) Variation in PL QY_{abs}, b) Emission spectra for the different (TEOS/MTEOS)/RB sols (λ_{exc} = 365 nm).

For all three wavelengths of interest, PL QY_{abs} (Fig. 3a) evolves similarly with an increasing RB concentration in TEOS/MTEOS sol, and this evolution is analogous to that described previously for RB in ethanol (Fig. 2b). However, the best PL QY_{abs} is not recorded for the same RB concentration. The higher viscosity of the TEOS/MTEOS/Ethanol sol promotes the distance between the RB molecules, which enables us to work with a higher concentration of emitting centres (3.29 10^{-4} mol/L in the TEOS/MTEOS sol compared to 1.65 10^{-4} for the ethanol solution) before observing an extinction by concentration.

As shown in Fig. S4b, absorbance increases with the amount of RB for the three excitation wavelengths, 275, 365 and 450 nm, while an increase in the internal quantum yield with the RB concentration is observed before reaching a threshold and then decreasing again, due to the concentration quenching phenomenon (Fig. S4a).

PL QY_{abs} is the product of PL QY_{int} and Abs; as mentioned before, the optimal optical yield results from the best matching between these two parameters.

RB ethanolic solutions and (TEOS/MTEOS)/RB sols are distinguished by a significant difference in viscosity (1.2 mPa.s and 17 mPa.s, respectively) which may explain the differences in behaviour recorded as a function of RB concentration in these two media.

The emission spectra recorded under excitation at 365 nm for the different (TEOS/MTEOS)/RB sols studied are presented in Fig. 3b. The spectral profile remains the same for all the sols and is characterized by a broad dissymmetric emission band situated between 550 and 750 nm. As observed for RB solutions in ethanol (Fig. S5), a shift of the emission band towards shorter wavelengths is observed as RB concentration decreases. These

observations reveal the presence of luminescence contributions that are possibly attributed to specific forms of the RB dye (monomer, dimer etc..). From a Gaussian-type deconvolution of the emission spectrum of samples S_{1T} and S_{2T}, which have the best PL QY_{abs} for the three excitation wavelengths studied (all the emission spectra were deconvoluted in the same way), three contributions are clearly identified (Fig. 4b and 4c in blue) and are reported in Table 3 (Area: integrate area under the curves, FWHM: Full Width at Half Maximum).

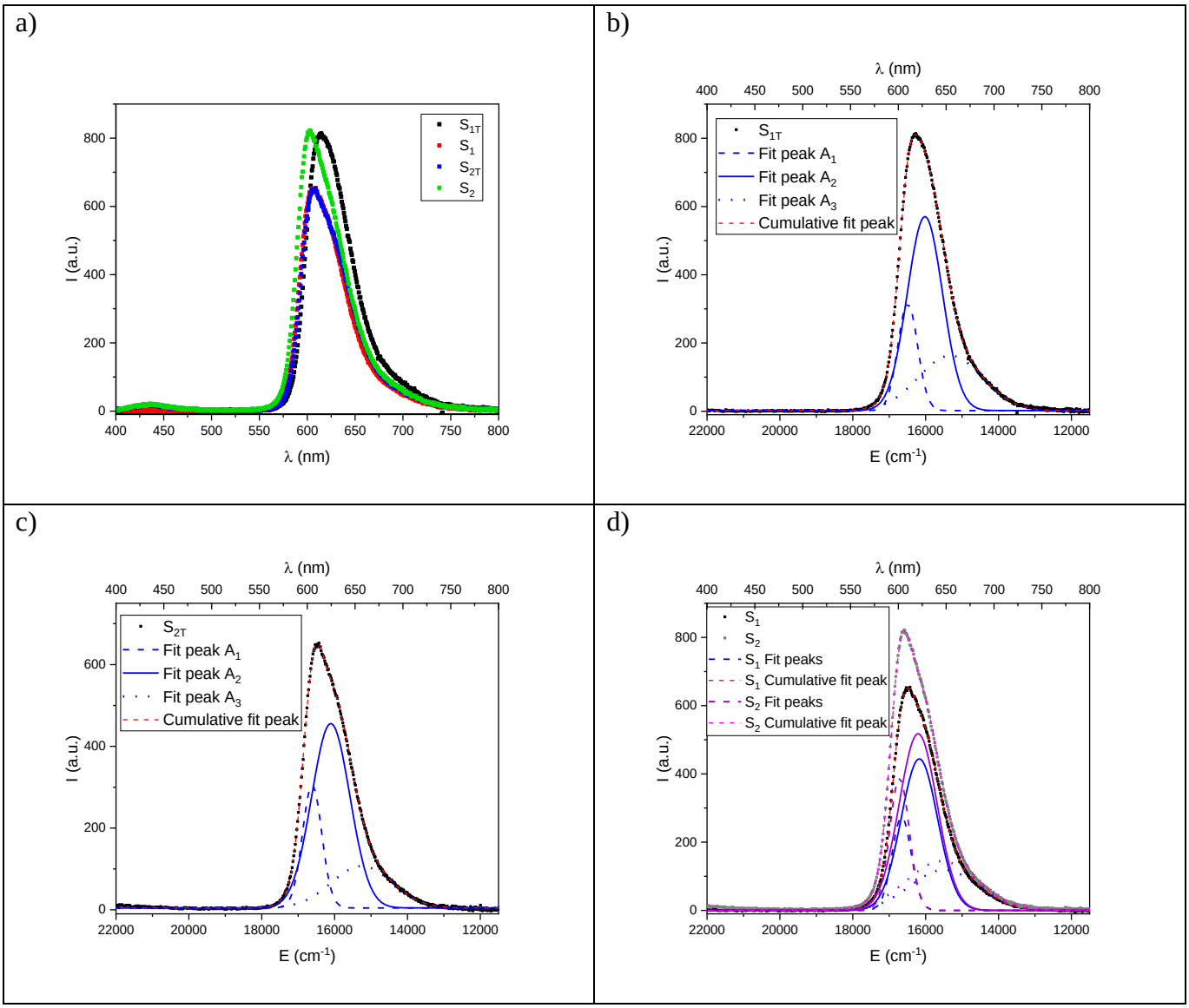

Fig. 4. a) Emission spectra of sols S_{1T}, S_{2T} and solutions S_1 and S_2 under excitation at 365 nm; b), c) and d) Gaussian-type deconvolution for S_{1T}, S_{2T} and S_1, S_2 respectively.

Table 3 Deconvolution of the emission spectra shown in Fig. 4a (λ_{exc} = 365 nm) (FWHM: Full Width at Half Maximum).

	Contribution A_n (n=1, 2 or 3)	E_{max} (cm^{-1})/λ_{max} (nm)	Area (a.u.)	FWHM (cm^{-1})
S_{1T}	1	16492 cm^{-1} (606 nm)	214022	639 cm^{-1}
	2	16020 cm^{-1} (624 nm)	689090	1139 cm^{-1}
	3	15320 cm^{-1} (652 nm)	354285	2062 cm^{-1}
S_{2T}	1	16616 cm^{-1} (601 nm)	199929	625 cm^{-1}
	2	16104 cm^{-1} (620 nm)	593364	1236 cm^{-1}
	3	15255 cm^{-1} (655 nm)	213452	1956 cm^{-1}
S_1	1	16659 cm^{-1} (600 nm)	181588	623 cm^{-1}
	2	16173 cm^{-1} (618 nm)	557952	1181 cm^{-1}
	3	15492 cm^{-1} (645 nm)	277518	2193 cm^{-1}
S_2	1	16718 cm^{-1} (598 nm)	261454	634 cm^{-1}
	2	16205 cm^{-1} (617 nm)	673106	1221 cm^{-1}
	3	15555 cm^{-1} (642 nm)	351642	2286 cm^{-1}

These emission spectra underline that an aggregation is evinced for a very low RB content in TEOS/MTEOS; this behaviour is similar to that described for fluorescein, where J and/or H type aggregates were also observed for very low dye concentrations.

Contribution 1 at high energy (lower wavelength) is attributed to RB being present as an isolated molecule (monomer), whereas contributions 2 and 3 are ascribed to aggregated forms of RB (dimer, trimer...). Measuring the contribution area A_1 for contribution 1, and so on, the ratio $A_1/\Sigma A$ ($A_1+A_2+A_3$) reveals the dispersion rate of the RB molecules in the dispersion media. The greater the ratio value is, the better the RB molecules are dispersed. Quantitatively, this ratio is found to increase with dilution, with A_1 representing about 20 % of the total contribution for sol S_{2T} and only 17% for the most concentrated sol S_{1T}, thus indicating that RB molecules are less likely to aggregate when present in small quantities. Although emission spectra deconvolutions for S_{3T} and S_{4T} (λ_{exc} = 365 nm) could not be performed due to the low emission intensity of these spectra, as shown in Fig. 3d, the deconvolution results of the S_{0T} emission spectrum with an even lower $A_1/\Sigma A$ ratio (0.1) than that recorded for the S_{1T} sol (Figure S6 and Table S1) confirms the importance of working with a low concentration to limit the aggregation of RB molecules.

These results were compared to those of RB in ethanol for the same RB concentration (Fig. 4d and Table 3); ratio $A_1/A_{n\ (n=1+2+3)}$ is equal to 0.18 and 0.2 for S_1 and S_2 respectively, compared to 0.17 and 0.2 for S_{1T} and S_{2T} respectively. We note that for these RB concentrations (3.29 10^{-4} and 1.65 10^{-4} mol/L) the chosen dilution media (ethanol or TEOS/MTEOS mixture) does not have a significant influence on the emission spectral profile. This is reflected by similar emission spectra, as shown in Fig. 4a. This results in very similar colour points, as shown in Fig. 4a and 5.

A change in the colour point (Fig. 5) is observed with the concentration of RB in the TEOS/MTEOS sol, i.e. the higher the RB concentration, the more the emission colour is red-shifted. This change in emission colour as a function of dye concentration is in agreement with the emission spectra in Fig. 3d and can be explained, as we have highlighted, by a reduction in the ratio of monomeric to aggregated forms of RB in the TEOS/MTEOS sol with increasing RB concentration. The same trend has been reported previously for RB and a series of LDH hybrid phases hosting fluorescein molecules [12,13].

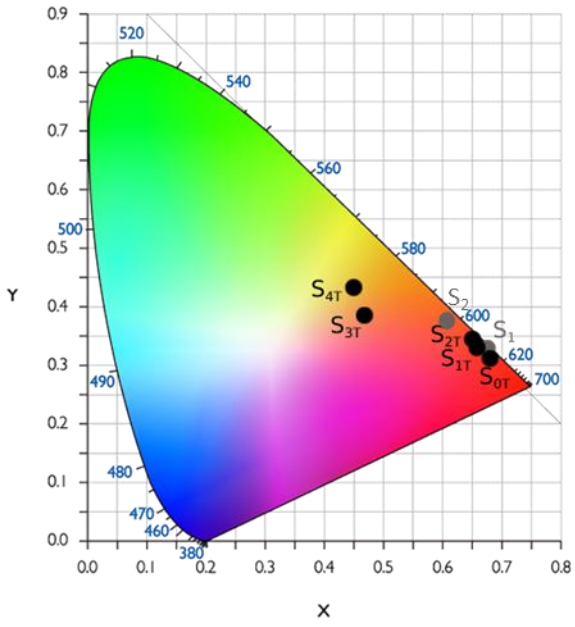

Fig. 5. CIE chromaticity coordinates of sol $S_{nT\ (n = 0,1,2,3\ and\ 4),}$ and of solutions S_1 and S_2.

The S_{1T} sol, exhibiting the best PL QY_{abs} under excitation at 365 nm, was used to produce thin films (labelled S_{1TR}) on quartz and silicon substrates by spin coating under the conditions described in the experimental section.

3.2. Characterisation of thin films (TEOS/MTEOS)/RB elaborated using spin coating

3.2.1. Physico-chemical characterizations

The thin film thickness on both substrates, quartz and silicon (the latter was used to enable the measurement of the refractive index), was measured by profilometry. The formulation and the viscosity of the (TEOS/MTEOS)/RB sol S_{1T} enabled a thickness in accordance with the specifications: 130 ± 20 nm with reproducible values for several experiments. The refractive index, determined by ellipsometry on the thin film made on a silicon substrate, was about 1.5.

The S_{1TR} composite film was also studied by atomic force microscopy (AFM). Fig. 6a, 6c and 6d show AFM height images of the (TEOS/MTEOS)/RB film as well as a phase image (Fig. 6d – right), while Fig. 6b shows an AFM image of the coatings without RB. These films were made under exactly the same conditions.

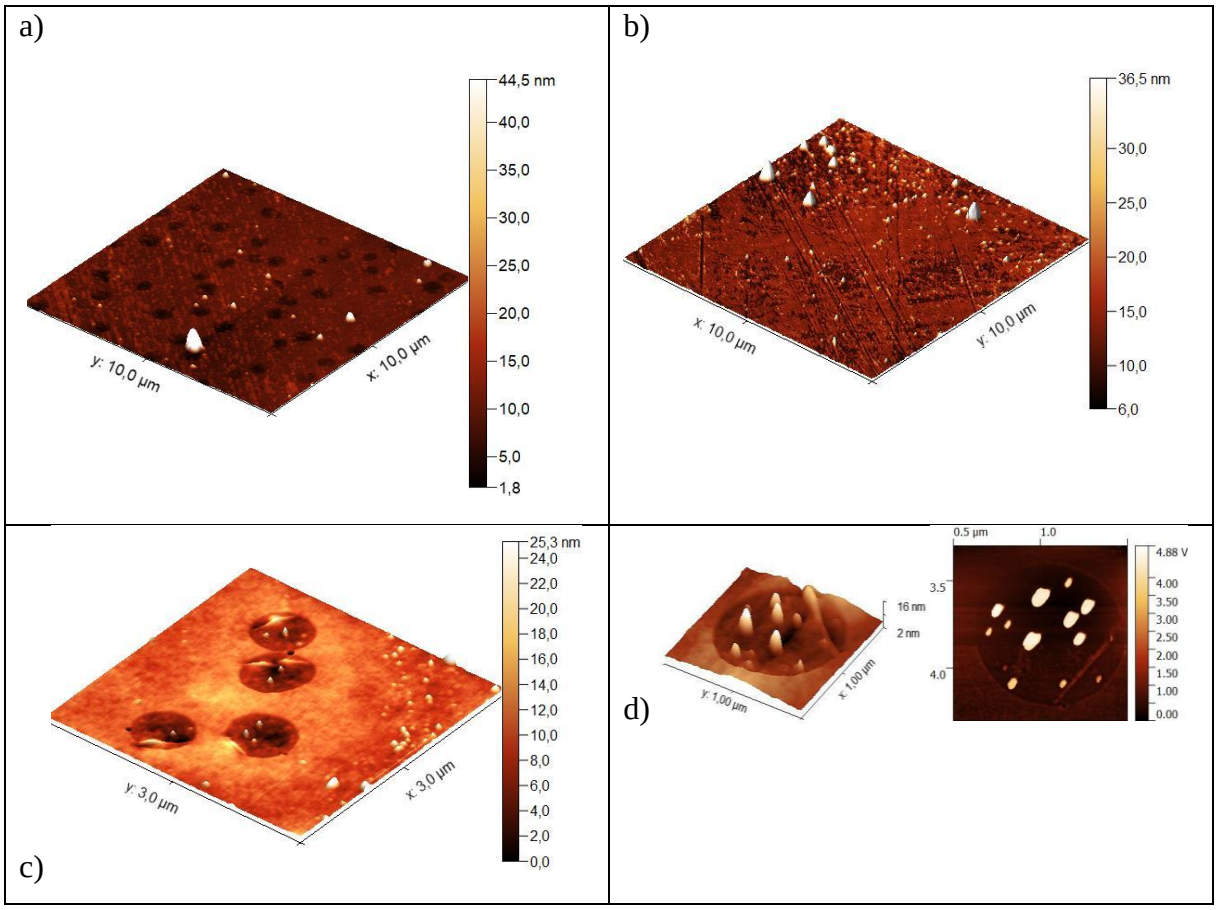

Fig. 6. AFM height images of a), c) and d) (TEOS/MTEOS)/RB film, b) TEOS/MTEOS film, c) AFM phase image of (TEOS/MTEOS)/RB film.

Low roughness was measured for both samples: its value was around 5 nm for the sample without RB, and remained almost unchanged when RB was added to the formulated sol (4.5 nm). RB chromophore seems to be incorporated into craters with well-defined shapes,

as shown in Fig. 6c and 6d. Indeed, the phase image shown in Fig. 6d enables RB particles to be distinguished from the sol-gel matrix. This gathering of luminescent particles into cells has already been observed in another kind of luminescent nanocomposite (polymer/phosphors) [16]. These craters are homogeneously distributed on the coating surface and present an average diameter of 700 nm. This homogeneous distribution of RB chromophore over the whole coating corroborates emission spectra features measured on coatings shown hereafter in which non-aggregated forms are favoured (Fig. 7).

3.2.1. Optical characterizations

The emission spectrum of the S_{1TR} coating developed by spin coating on a quartz substrate was recorded as for the S_{1T} sol under excitation at 365 nm. The latter is characterized (Fig. 7) by an asymmetric profile that can be associated with the different contributions of monomeric and aggregated RB. A significant shift (≈ 40 nm) of the emission maximum towards the short wavelength side of the spectrum is observed for S_{1TR} compared to the S_{1T} sol. Furthermore, the deconvolution of the S_{1TR} emission spectrum (Fig. 8 and Table 4) shows a very high ratio A_1/A_1+A_2 (0.6) compared to that recorded for the S_{1T} sol (0.2), indicating that in the film the RB molecules are better dispersed and isolated from each other (a deconvolution by the sum of 3 Gaussian functions did not lead to a consistent result, which is justified by the very small contribution of the aggregated forms as we have shown). As mentioned above, this result is quite consistent with the AFM observation, where a very homogeneous distribution of RB in the silica lattice was revealed.

a)

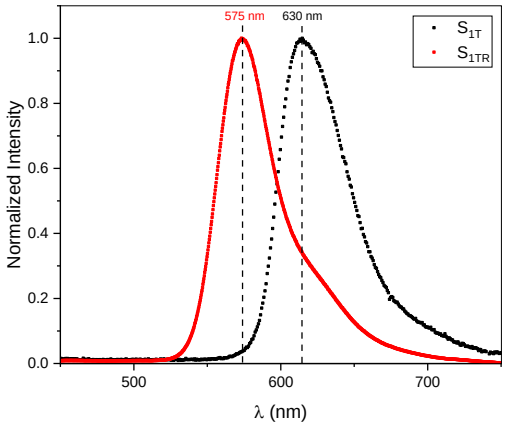

b)

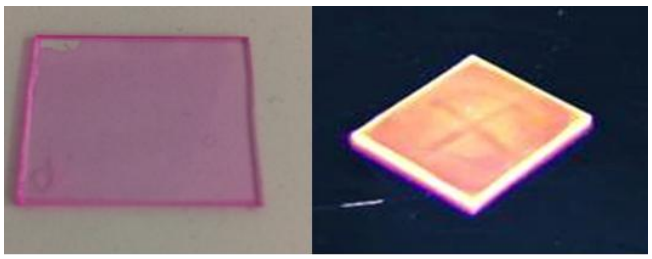

daylight

uder UV light
λ =365 nm

Fig. 7. a) Normalized emission spectra of the thin film S_{ITR} deposited on a quartz substrate (solid line) and of the sol S_{1T} (dotted line) under excitation at 365 nm, b) Photograph of the S_{1TR} luminescent coating applied to a quartz substrate under daylight and excitation at 365 nm.

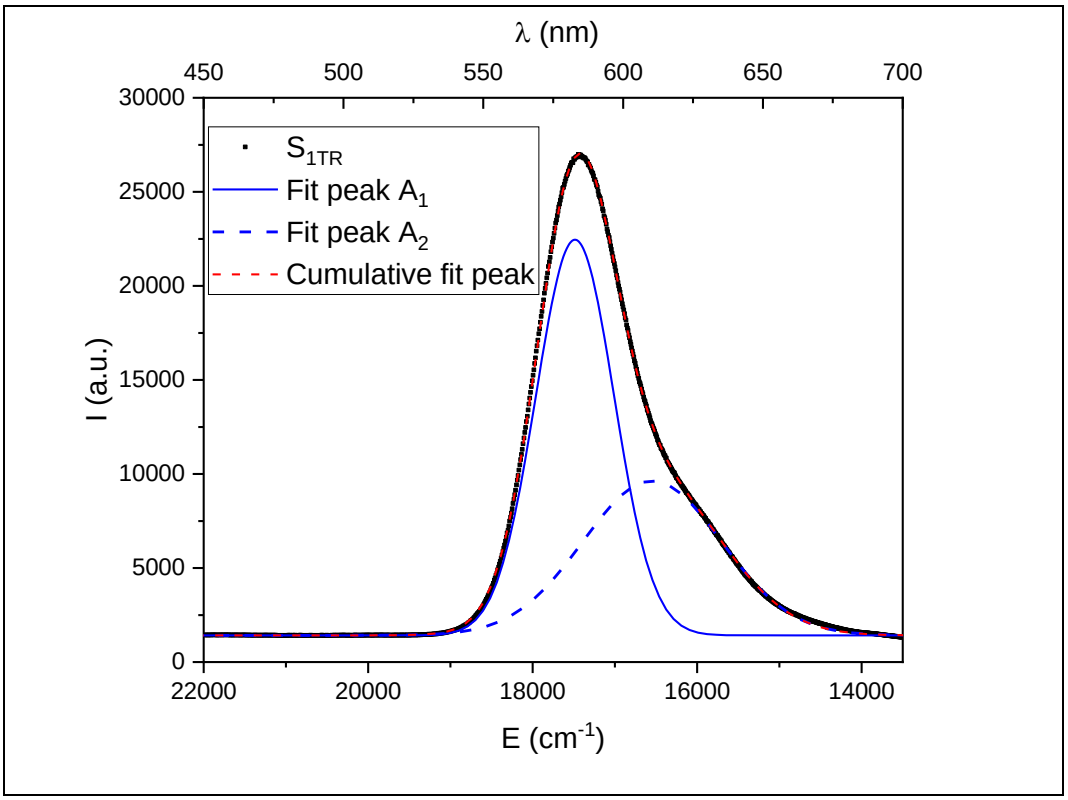

Fig. 8. Gaussian-type deconvolution for S_{1TR} (λ_{exc} = 365 nm).

Table 4 Deconvolution of the emission spectra S_{1TR} (λ_{exc} = 365 nm) (FWHM: Full Width at Half Maximum).

	Contribution	E_{max} (cm^{-1})/λ_{max} (nm)	Area (a.u.)	FWHM (cm^{-1})
S_{1TR}	1	17485 cm^{-1} (571 nm)	$2.5\ 10^7$	1117 cm^{-1}
	2	16545 cm^{-1} (604 nm)	$1.7\ 10^7$	1989 cm^{-1}

3.3. Combination of a diffraction grating and the luminescent coating.

3.3.1 Physico-chemical characterisation

Sample S_{1TR} was embossed to create a grating on the luminescent coating (S_{1TRE}). Fig. 9 shows the 3D AFM image of sample S_{1TRE}.

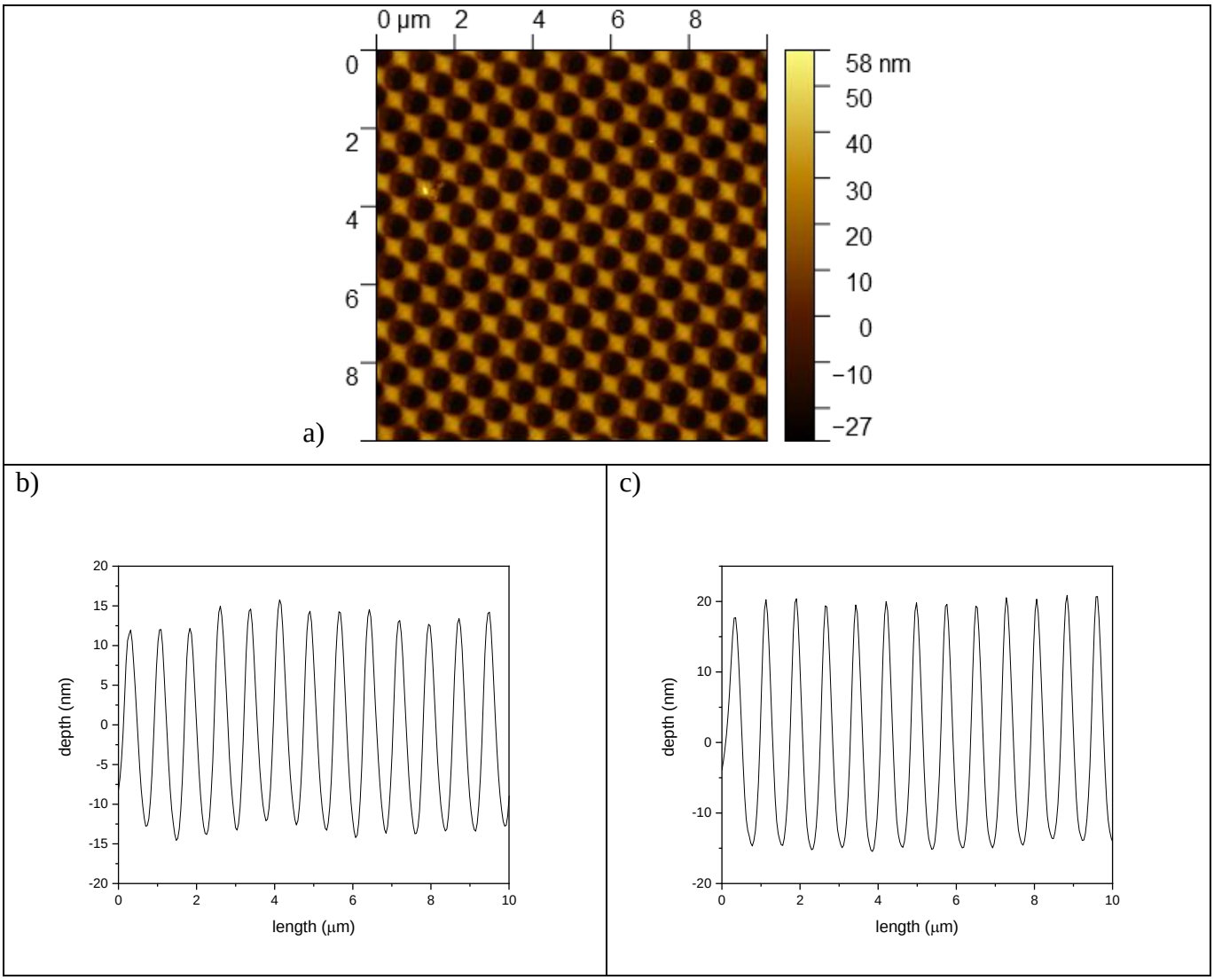

Fig. 9. a) AFM image of (TEOS/MTEOS)/RB embossed film (S_{1TRE}); b) and c) AFM profile in two perpendicular directions of (TEOS/MTEOS)/RB embossed film (S_{1TRE}).

A 2D grating is observed with a period of 950 nm for an average depth of 35 nm. The grating profile is close to a sine curve, giving the honeycomb pattern in the image. The profiles are regular and homogeneous in the two directions, which will enable us to obtain reliable optical results for the next step. The craters where RB molecules are located are not visible; they are "erased" by the embossing of the sol-gel film because the size of these craters (Fig. 6) is less than 1 µm, corresponding roughly to the size of the grating period. This does not disturb the homogeneity of the grating.

3.3.2. Optical characterisations

Angle-resolved photoluminescence measurements, performed on samples S_{1TR} and S_{1TRE}, are shown in Fig. 10. The excitation wavelength is 375 nm with an incidence of 60°.

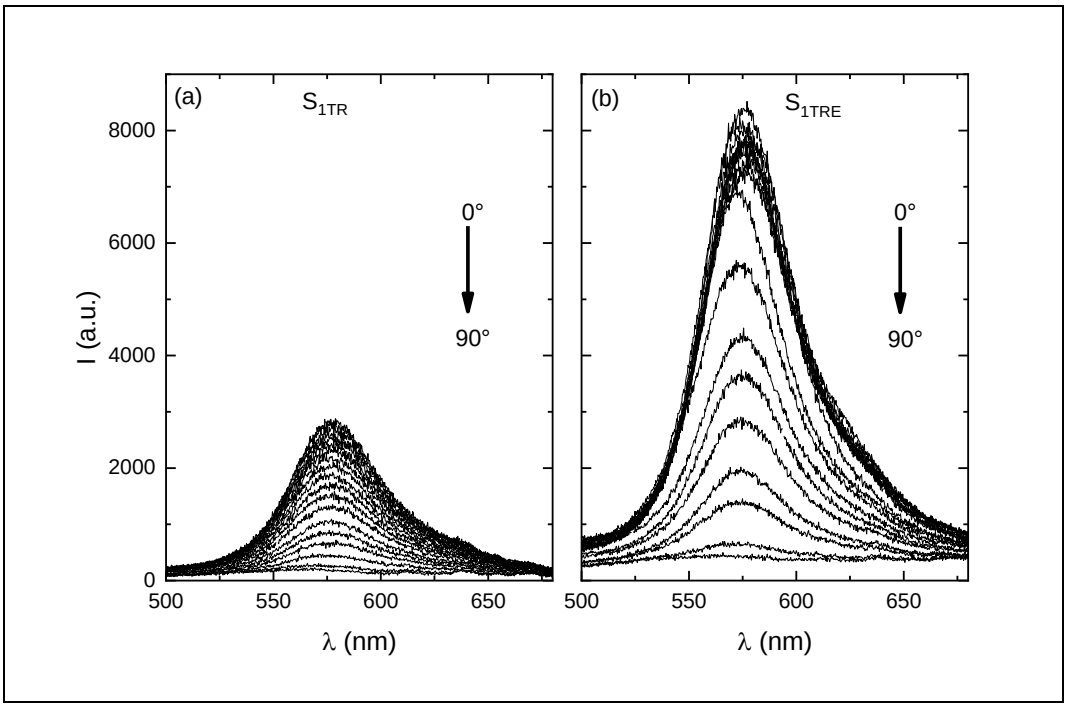

Fig. 10. Angle-resolved photoluminescence recorded from 0° to 90° on sample (a) S_{1TR} and (b) S_{1TRE} (λ_{exc} = 375 nm).

For both samples – plane and micro-structured – the emission spectra are centred around 575 nm and the shape is similar. Thanks to the presence of the 2D grating (S_{1TRE}), the emission intensity is 3 to 4 times higher in the 0°-75° range than for sample S_{1TR} (Fig. 11). The 2D grating strongly improves light extraction from the RB film. The maximum intensity measured at 575 nm is plotted in Fig. 11 as a function of the emission angle. Around 40°, a slight increase in emission intensity associated with a shift of 2-3 nm is observed.

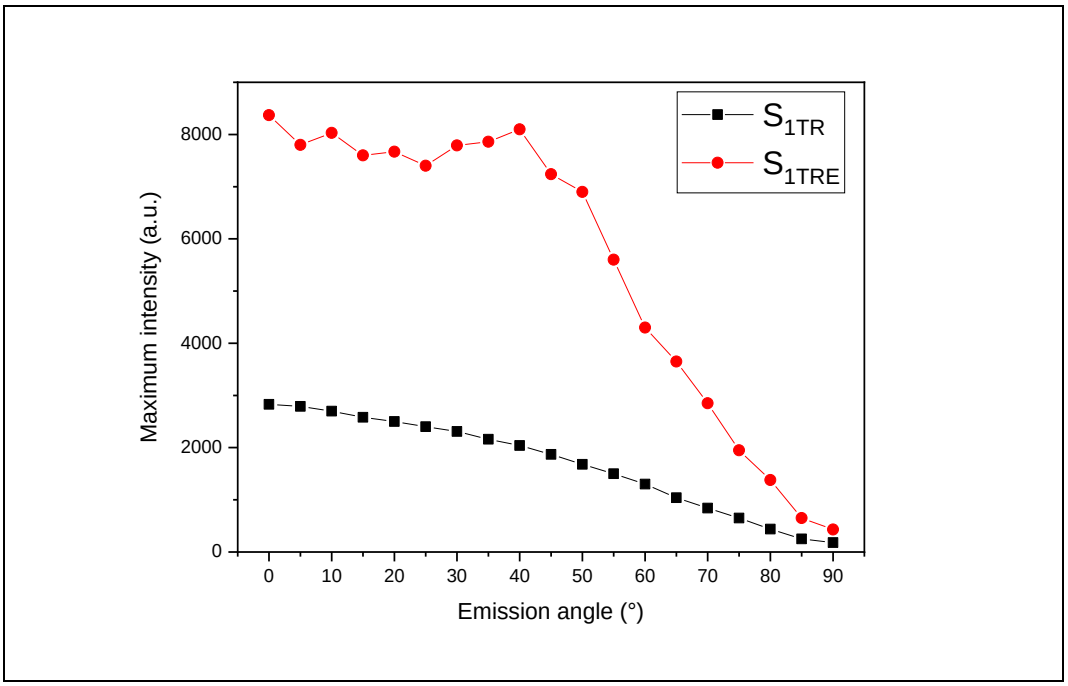

Fig. 11. Maximum emission intensity measured at 575 nm from Fig. 9 versus emission angle.

To investigate the dependent angular emission with a better resolution we used far-field emission measurements. Emission mappings of sample S_{1TRE} are plotted in Fig. 12. The behaviour observed in Fig. 9 is clearly evidenced in Fig. 12a. RB emission filtered by 2D grating exhibits a second maximum around 40°. This resonant effect depends on the light polarization. It is completely turned off in vertical polarization (Fig. 12b) while it is clearly evidenced in horizontal polarization (Fig. 12c).

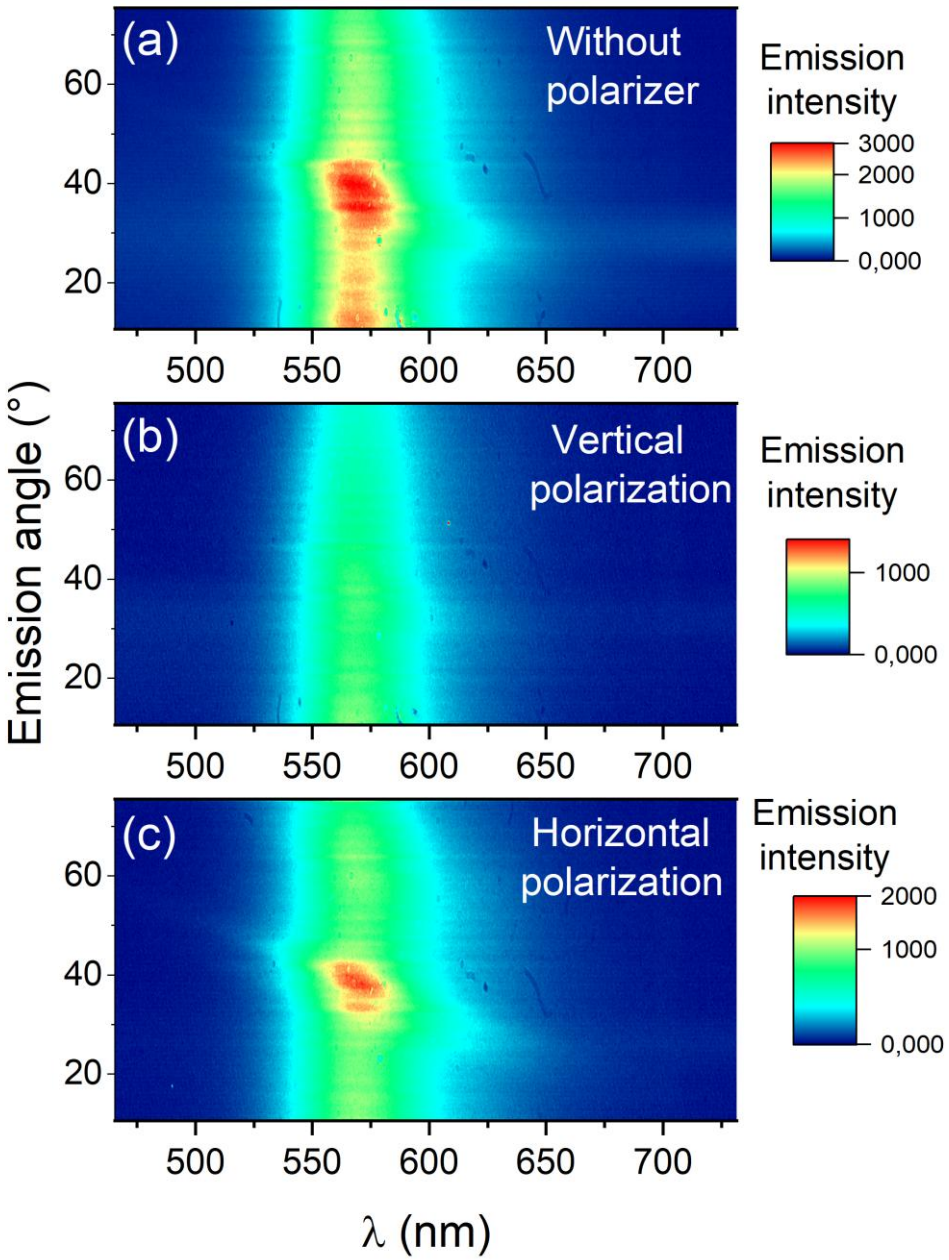

Fig. 12. Far-field emission measurements of sample S_{T1RE} (a) without polarizer, (b) in vertical polarization and (c) in horizontal polarization.

Conclusion

This study presents the interest of fabricating an embossed luminescent sol-gel coating, which provides a significant increase in luminescence over the structured areas. We have demonstrated that our sol-gel is compatible with the nanoimprint method and that the

optical properties of the luminescent matrix (RB) are safeguarded. The surface structuring obtained is homogeneous and regular. A significant improvement in luminescence with the structuring, as well as a grating effect where the light seems to favour one direction, are highlighted. Prospects now envisaged include improving this performance in order to maximize its effect, and working with patterns in order to make the approach attractive for the field of anti-counterfeiting technology.

Acknowledgments

The authors would like to thank the Auvergne Rhône Alpes Region for funding this thesis as part of the LUEUR project (Pack Ambition Recherche). This work was partly supported by the CNRS French Renatech Network, within the technological platform NanoSaintEtienne.

Authors acknowledge Hugo Bruhier for his technical support and expertise on AFM analyses.

Declaration of Competing Interest

The authors declare that they have no known competing financial interests or personal relationships that could have appeared to influence the work reported in this paper.

References

[1] A. Abdollahi, H. Roghani-Mamaqani, B. Razavi, M. Salami-Kalajahi, Photoluminescent and Chromic Nanomaterials for Anticounterfeiting Technologies: Recent Advances and Future Challenges, ACS Nano 14 (2020) 14417-14492. doi: 10.1021/acsnano.0c07289.

[2] J. Sauvage-Vincent, S. Tonchev, C. Veillas, S. Reynaud, Y. Jourlin, Optical security device for document protection using plasmon resonant transmission through a thin corrugated metallic film embedded in a plastic foil, JEOS:RP 8 (2013) 13015. doi: 10.2971/jeos.2013.13015.

[3] K. Kobayashi, N. Sakai, S. Matsui, M. Nakagawa, Fluorescent UV-Curable Resists for UV Nanoimprint Lithography, Jpn. J. Appl. Phys. 49 (2010) 06GL07. doi: 10.1143/JJAP.49.06GL07.

[4] H. Hauser, B. Herter, C. L. M. Hofmann, O. Höhn, V. Kübler, S. Fischer, S. Wolf, S. Fasold, F. C. J. M. van Veggel, J. C. Goldschmidt, B. Bläsi, Soft thermal nanoimprint of PMMA doped with upconverter nanoparticles, Microelec. Eng. 187–188 (2018) 154-159. doi: 10.1016/j.mee.2017.11.004.

[5] C. Pina-Hernandez, A Koshelev, S. Dhuey, S. Sassolini, M. Sainato, S. Cabrini, K. Munechika, Nanoimprinted High-Refractive Index Active Photonic Nanostructures Based on

Quantum Dots for Visible Light, Sci. Rep. 7 (2017) 17645. doi: 10.1038/s41598-017-17732-0.

[6] D. Huh, W. Kim, K. Kim, S. Son, J. Park, S. Ju, D. Chae, S. Baek, H. Lee, Enhancing light conversion efficiency of YAG:Ce phosphor substrate using nanoimprinted functional structures, Nanotechnology 31 (2020) 144003. doi: 10.1088/1361-6528/ab667e.

[7] L. A. Muscarella, A. Cordaro, G. Krause, D. Pal, G. Grimaldi, L. S. D. Antony, D. Langhorst, A. Callies, B. Bläsi, O. Höhn, A. F. Koenderink, A. Polman, B. Ehrler, Nanopatterning of Perovskite Thin Films for Enhanced and Directional Light Emission, ACS Appl. Mater. Inter. 14 (2022) 38067-38076. doi: 10.1021/acsami.2c09643.

[8] A. Revaux, G. Dantelle, D. Decanini, F. Guillemot, A.-M. Haghiri-Gosnet, C. Weisbuch, J.-P. Boilot, T. Gacoin, H. Benisty, Photonic crystal patterning of luminescent sol–gel films for light extraction, Nanotechnology 22 (2011) 365701. doi: 10.1088/0957-4484/22/36/365701.

[9] S. Anastasova, M. Milanova, S. Rangelov, D. Todorovsky, Influence of the precursor nature and deposition mode on the oxygen sensing properties of Ru(II) complex immobilized in a SiO2-based matrix, J. Non-Cryst. Solids 354 (2008) 4909-4916. doi: 10.1016/j.jnoncrysol.2008.07.006.

[10] X. Rios, P. Moriones, J. C. Echeverría, A. Luquín, M. Laguna, J. J. Garrido, Characterisation of hybrid xerogels synthesised in acid media using methyltriethoxysilane (MTEOS) and tetraethoxysilane (TEOS) as precursors, Adsorption 17 (2011) 583-593. doi: 10.1007/s10450-011-9331-9.

[11] A. A. M. Farag, I. S. Yahia, Rectification and barrier height inhomogeneous in Rhodamine B based organic Schottky diode, Synth. Met. 161 (2011) 32-39. doi: 10.1016/j.synthmet.2010.10.030.

[12] P. Legentil, F. Leroux, S. Therias, D. Boyer, G. Chadeyron, Sulforhodamine B-LDH composite as a rare-earth-free red-emitting phosphor for LED lighting, J. Mater. Chem. C 8 (2020) 11906 -11915. doi: 10.1039/D0TC02802A.

[13] P. Legentil, F. Leroux, S. Therias, R. Mahiou, G. Chadeyron, Revisiting fluorescein and layered double hydroxide using a synergistic approach: A complete optical study, J. Lumin. 215 (2019) 116634. doi: 10.1016/j.jlumin.2019.116634.

[14] S. De, R. Kundu, Spectroscopic studies with fluorescein dye—Protonation, aggregation and interaction with nanoparticles, J. Photochem. Photobiol. A: Chemistry 223 (2011) 71-81. doi: 10.1016/j.jphotochem.2011.07.002.

[15] S. Das, A. P. Chattopadhyay, S. De, Controlling J aggregation in fluorescein by bile salt hydrogels, J. Photochem. Photobiol. A: Chemistry 197 (2008) 402-414. doi: 10.1016/j.jphotochem.2008.02.003.
[16] A. Potdevin, G. Chadeyron, S. Thérias, R. Mahiou, Luminescent Nanocomposites Made of Finely Dispersed $Y_3Ga_5O_{12}$:Tb Powder in a Polymer Matrix: Promising Candidates for Optical Devices, Langmuir 28 (2012) 13526-13535. doi: 10.1021/la302816w.